

See discussions, stats, and author profiles for this publication at: <https://www.researchgate.net/publication/263990807>

Two Chain-Packing Transformations and Their Effects on the Molecular Dynamics and Thermal Properties of α -Form Isotactic Poly(propylene) under Hot Drawing: A Solid-State NMR Study

ARTICLE *in* MACROMOLECULES · APRIL 2014

Impact Factor: 5.8 · DOI: 10.1021/ma5004369

CITATIONS

3

READS

9

2 AUTHORS, INCLUDING:



Jia Kang

University of Akron

5 PUBLICATIONS 5 CITATIONS

SEE PROFILE

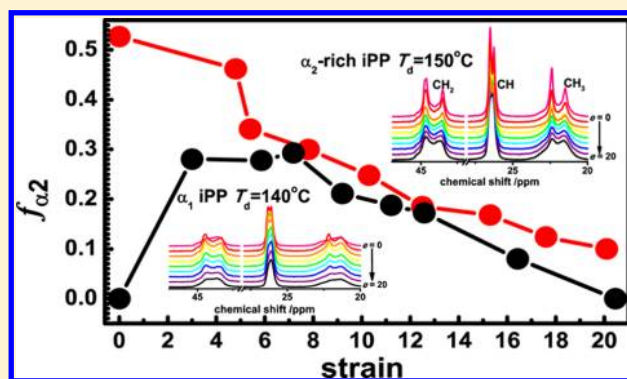
Two Chain-Packing Transformations and Their Effects on the Molecular Dynamics and Thermal Properties of α -Form Isotactic Poly(propylene) under Hot Drawing: A Solid-State NMR Study

Jia Kang and Toshikazu Miyoshi*

Department of Polymer Science, The University of Akron, Akron, Ohio 44325-3909, United States

S Supporting Information

ABSTRACT: The chain packing, crystal thickness, molecular dynamics, and melting temperature of α -form isotactic polypropylene (*i*PP) drawn uniaxially at high temperatures of 100–150 °C were investigated using solid-state (SS) NMR and DSC. Two types of *i*PP samples with disordered (α_1) and relatively ordered (α_2 -rich) packing structures were prepared via different thermal treatments and drawn up to an engineering strain (ϵ) of approximately 20. High-resolution ^{13}C NMR detected continuous $\alpha_2 \rightarrow \alpha_1$ transformations in the original α_2 -rich samples over the entire deformation range at all drawing temperatures (T_d s). A sudden $\alpha_1 \rightarrow \alpha_2$ transformation was found to occur in the original α_1 sample in the small ϵ range of approximately 3–7 at $T_d = 140$ °C. Then, in the late stage, the newly grown α_2 structure reversely transformed into α_1 structure with further increase in ϵ , as observed in the original α_2 -rich sample. These results indicate that at least two different processes are involved in large deformations. On the basis of crystallographic constraints, the continuous $\alpha_2 \rightarrow \alpha_1$ transformation over the entire deformation range is attributed to molecular-level melting and recrystallization facilitated by chain diffusion. The steep $\alpha_1 \rightarrow \alpha_2$ transformation in the smaller ϵ range is assigned to isotropic melting and recrystallization induced by stress. After the large deformations ($\epsilon \approx 20$) of the original α_2 -rich and α_1 samples at $T_d = 150$ and 140 °C, respectively, ^1H spin diffusion verified increases in the crystal thickness in both the former (14.1 at $\epsilon = 0 \rightarrow 20.1$ nm at $\epsilon = 20$) and the latter (9.2 \rightarrow 17.0 nm). Centerband-only detection of exchange (CODEX) NMR at 120 °C demonstrated that the correlation time ($\langle\tau_c\rangle$) of the helical jump for the former drastically decreased from $\langle\tau_c\rangle = 52.4 \pm 5.2$ at $\epsilon = 0$ to 9.3 ± 1.8 ms at $\epsilon = 20$ but slightly increased from 4.2 ± 1.3 to 7.1 ± 0.9 ms for the latter. Additionally, DSC indicated that the melting temperature (T_m) for the former decreased considerably from 173 °C at $\epsilon = 0$ to 165 °C at $\epsilon = 20$, whereas the melting temperature (T_m) remained nearly invariant at 163 °C for the latter. On the basis of these findings, we conclude that the local packing structure plays a crucial role in determining the molecular dynamics of the stems and T_m of largely deformed *i*PP materials. The established relations among the structures, the dynamics, and the thermal properties provide a useful guide to achieving improved properties of *i*PP materials under processing.



1. INTRODUCTION

The deformation of semicrystalline polymers is inevitable during polymer processing and the daily use of polymeric material. The simplest deformation process, uniaxial drawing, orients molecular chains along the direction of drawing and modifies the hierarchical crystalline structures,^{1–24} which in turn significantly influences the mechanical properties of the semicrystalline polymers.^{25–27} Therefore, it is of great interest and practical importance to understand how crystalline structures evolve on various length scales upon uniaxial drawing and how the new structures induced by this process are related to the molecular dynamics and bulk properties of the materials.

Two prevailing mechanisms are used to explain the deformation of semicrystalline polymers. One mechanism is the three-stage model, which includes rotation, sliding, and

fragmentation of lamellae in stage I, incorporation of the fragmented blocks into microfibrils in stage II, and longitudinal sliding of the microfibrils in stage III.¹ These structural evolutions have been well characterized using various tools, such as transmission electron microscopy (TEM),^{2–4} atomic force microscopy (AFM),⁵ polarized optical microscopy (POM),⁶ IR spectroscopy,⁷ X-ray diffraction (XRD),^{8–10} and small-angle X-ray scattering (SAXS).^{6,8–12} The other mechanism is melting and recrystallization.¹³ Neutron scattering (NS) has permitted the observation of the isotopic segregation of crystallized polyethylene (PE) and deuterated PE (DPE) blends under tensile drawing at temperatures above approx-

Received: February 26, 2014

Revised: April 8, 2014

Published: April 16, 2014

imately 60 °C,¹⁴ but not in the further drawing of already necked samples.^{15,16} The segregation of PE and DPE is direct evidence of local melting and recrystallization in the early stages of deformation.^{14,17}

Beyond the two prevailing mechanisms, Takayanagi et al. have interpreted the drawability of semicrystalline polymers in terms of the molecular motions related to the α relaxation of crystalline regions (α_c).¹⁸ This explanation is reasonable because certain semicrystalline polymers such as PE,²⁸ isotactic polypropylene (iPP),²⁹ poly(ethylene oxide) (PEO),³⁰ poly(oxyethylene) (POM),³¹ and isotactic poly(4-methyl-1-pentene) (iP4M1P)³² exhibit ultradrawability (engineering strain, $\epsilon > 20$) at temperatures above their α_c relaxation temperatures. Developments in one- and two-dimensional exchange solid-state (SS) NMR have directly revealed that the origin of α_c relaxations is large-amplitude motions of the stems in semicrystalline polymers that induce chain diffusions.^{33–38} Hu and Schmidt-Rohr have categorized such semicrystalline polymers as “ α_c -mobile crystals”.³⁹ However, it has been experimentally difficult to observe the effects of the molecular dynamics on any detectable structures. Chain diffusion therefore remains unrecognized as a primary deformation mechanism for semicrystalline polymers.

Among the various semicrystalline polymers, iPP is one of the most widely used industrial materials and has thus been extensively investigated in the field of deformation study.^{6–10,19–21} When iPP melt is cooled down, the melt crystallizes in the α form.⁴⁰ The α form is further divided into α_1 and α_2 , according to different degrees of order in the up/down orientations of the methyl groups. The arrangement of the methyl-group orientations, which are determined by the backbone conformations, is statistically disordered in the α_1 form but completely ordered in the α_2 form. Rapid crystallization at low temperatures kinetically favors the disordered α_1 structure, whereas slow crystallization at high temperatures favors the thermodynamically stable α_2 structure.^{41,42} Annealing of the disordered α_1 structure above 150 °C leads to partial transformation into α_2 structures.^{43,44} XRD and SS-NMR can distinguish the ordered packing structure from the disordered packing structure.^{41–45} Recently, high-resolution ¹³C SS-NMR under a very powerful decoupling sequence⁴⁶ has permitted improvement of the spectral resolution of the crystal signals and the quantitative evaluation of the order–disorder phenomenon of chain packing as a function of the crystallization and annealing temperatures (T_c and T_a).^{47,48} Moreover, SS-NMR studies have reported that large-amplitude motions of crystalline chains in quiescent-crystallized samples strongly depend on both the lamellar thickness and the packing structure (α_1 vs α_2).⁴⁷

In this work, we investigate the chain-packing structure, molecular dynamics, and melting temperature (T_m) of initially α_1 and α_2 -rich iPP samples deformed under hot drawing using various SS-NMR techniques. Our first goal is to understand the deformation mechanism at the molecular level by tracing the local packing changes in two iPP samples via high-resolution ¹³C SS-NMR. High-resolution NMR can clearly detect unique and complex transformations depending on the initial structures, the drawing temperatures (T_d), and the engineering strains (ϵ). The observed structural changes cannot be explained using the three-stage model but can be reasonably interpreted in terms of two different melting and recrystallization processes on different length scales and in different deformation ranges. Our second goal is to elucidate how

deformed structures influence the molecular dynamics and T_m of largely drawn iPP samples. The crystal thicknesses, the helical jump motions of the crystalline stems, and the melting behavior of undrawn and drawn iPP samples are investigated via ¹³C-detected ¹H spin diffusion, centerband-only detection of exchange (CODEX) NMR,³⁷ and DSC, respectively. Through these systematic investigations as well as by considering the packing structures, we establish specific correlations between the hierarchical structures with molecular dynamics and thermal properties.

2. MATERIALS AND EXPERIMENTS

2.1. Sample Preparation. Commercially available iPP with a weight-averaged molecular weight of 340 000 and a polydispersity of 3.5 was purchased from Sigma-Aldrich Co. iPP samples with two different crystalline forms (α_1 and α_2 -rich) were prepared from the original pellets. An inhibitor, 2,6-di-*tert*-butyl-4-methylphenol (BHT), was dissolved in acetone and dispersed onto the iPP before sample processing to avoid oxidation at high temperatures (BHT:iPP = 0.1 wt %). The iPP pellets were premelted at 220 °C, molded at the same temperature using a compression-molding machine, and subsequently quenched in icy water. The iPP plates obtained in this manner (160 × 160 × 2 mm) were annealed in a vacuum oven at 100 °C for 2 h to prepare the α_1 sample. The α_2 -rich sample was obtained by further annealing a α_1 sample at 165 °C for 72 h under vacuum. The plates were cut into a dumbbell shape with the type V cutter required by the American Standards of Testing Materials (ASTM) D638. The tensile stretching of the dumbbell-shaped iPP specimens was performed using a computer-interfaced Instron 5567 apparatus with a temperature-controlled chamber at a drawing rate of 10 mm/min. The T_d s were set to 100, 125, and 150 °C for the α_2 -rich sample, whereas the α_1 sample was stretched at 100, 125, and 140 °C to avoid complete melting (onset melting point of α_1 iPP = 151 °C, as determined via DSC). After reaching the target temperature, each sample remained in the temperature chamber for an additional 5 min to allow the system to stabilize before drawing. The temporary extension and load were obtained from the Instron software and converted into the engineering strain and stress, respectively. To avoid any overestimation of the engineering strain caused by slippage of the specimens between the clamps during drawing, two lines were marked on the gauge part, and the initial distance between the two lines was measured before the specimens were placed into the Instron. After drawing and the recovery of the specimens from elastic deformation, the final distance between the two lines was measured to calculate the final strain. For each specimen, drawing was terminated at various strains from 0 to approximately 20 at the given T_d s. We used freshly prepared samples for subsequent NMR experiments at ambient temperature.

2.2. SS-NMR. **2.2.1. CP and DPMAS.** SS-NMR experiments were conducted using a Bruker AVANCE 300 SS-NMR equipped with a 4 mm double-resonance VT CPMAS probe. The ¹H and ¹³C carrier frequencies were 300.1 and 75.6 MHz, respectively. The MAS frequency was set to 4000 ± 3 Hz. The ¹³C chemical shift was calibrated using the CH signal of adamantane (29.46 ppm) as an external reference. The ¹³C CPMAS NMR experiments and the measurements of the ¹H spin–lattice relaxation time in the rotating frame ($T_{\rho H}$) were conducted at ambient temperature. The 90° pulses for ¹H and ¹³C were adjusted to 4.5 μ s. The recycle delay and the cross-polarization (CP) time were 2 s and 1 ms, respectively. ¹H two pulse phase modulation (TPPM)⁴⁶ decoupling with a field strength of 100 kHz was applied during an acquisition time of 120 ms. A proton spin–lattice relaxation time in the rotating frame ($T_{\rho H}$) filter of 8 ms under a spin-locking (SL) field strength of 62.5 kHz was used for the selective observation of the pure crystalline signals. Direct polarization (DP) MAS experiments for determining the crystallinity were conducted using a 7 mm double-resonance VT CPMAS probe at 90 °C. The ¹³C spin–lattice relaxation time (T_{1C}) of the CH carbon in the crystalline region was determined to be 34 s at 90 °C. The recycle delay was set to 170 s. ¹H TPPM decoupling with a field strength of 50

kHz was applied during an acquisition time of 50 ms. The temperature inside the NMR probe was carefully calibrated using the temperature dependence of the ^{207}Pb chemical shift in $\text{Pb}(\text{NO}_3)_2$ powder.⁴⁹ One DPMAS experiment required 20 h.

2.2.2. Spin Diffusion.⁵⁰ A Goldman–Shen sequence consisting of three pulses combined with CP was applied to investigate the spin diffusion between the crystalline and amorphous regions at 90 °C. The ^1H spin–spin relaxation time (T_2) filter was set to 25 μs to suppress the original crystalline signals. Spin diffusion from the remaining amorphous magnetization to the crystalline magnetization was measured as a function of spin-diffusion time (t_{SD}) up to 1440 ms. To calibrate the T_1 relaxation effect during the t_{SD} , additional reference experiments without the T_2 delay were performed. Both the spin diffusion and reference experiments required 4 h.

2.2.3. CODEX.³⁷ CODEX experiments were performed to evaluate the correlation time (τ_c) of the helical jump of the iPP stems at 120 °C. The chemical-shift anisotropy (CSA) was recoupled via a series of 180° pulses in two evolution periods separated by a mixing time, t_{mix} . CODEX data were acquired under an MAS frequency of 4000 ± 3 Hz with an acquisition time of 90 ms. The ^1H rf field strengths for CW decoupling during the ^{13}C 180° pulse in the evolution periods and for TPPM decoupling during detection were set to 100 kHz. During the remaining evolution periods, CW decoupling with a strength of 86 kHz was applied. The evolution time for the CSA was set to 2 ms. The mixing time was varied from 0.25 to 2000 ms. The reference and exchange spectra were alternately obtained every 128 scans to avoid instability in the NMR spectrometer. Each spectrum was accumulated 1920 times. Typically, one t_{mix} dependence experiment required 31 h.

2.4. DSC Measurements. The first heating cycle of iPP samples of approximately 5 mg was performed using a computer-interfaced TA Instruments DSC Q2000 apparatus at a heating rate of 10 °C/min with a surrounding Ar atmosphere to avoid the thermal degradation of the iPP samples. Liquid nitrogen was used to control the cooling process. The temperature and heat flow were calibrated using standard materials before the iPP samples were tested.

2.5. SAXS Measurements. SAXS experiments of undrawn iPP samples were performed on a Rigaku MicroMax 002+ instrument equipped with a 2D multiwire area detector and a sealed copper tube at room temperature. The working voltage and current for the X-ray tube were 45 kV and 0.88 mA, respectively. The wavelength of the X-ray was 0.154 nm. The scattering vector (q) was calibrated using silver behenate with the primary reflection peak at $q = 1.067 \text{ nm}^{-1}$. The SAXS diffraction patterns covering the q range between 0.2 and 2.0 nm^{-1} were recorded. The recording time for each set of data was 5–10 min, depending on the scattering intensity. The background scattering was subtracted and further analyzed with the Rigaku software SAXSgui. Note that SAXS does not provide scattering peak for highly stretched iPP samples at ambient temperature.

3. RESULTS

3.1. ^{13}C CPMAS NMR Spectra of the α_1 and α_2 -Rich Samples. iPP chains adopt 3_1 helical conformations in crystalline regions. In the α form, 3_1 left- (L) and right-handed (R) helices are enmeshed into pairs within a bilayer along the a^* axis. In addition, the upward and downward orientations of the methyl groups allow the stems to choose either ordered or disordered packing structures. In the α_2 structure, the methyl groups have either complete upward or complete downward orientations within each bilayer (Figure 1a), whereas the α_1 form displays statistical disorder of the orientations at each site (Figure 1b).^{41,42} The ^{13}C CPMAS spectra of undrawn α_2 -rich iPP with (blue line) and without (purple line) a spin-locking time filter are depicted in Figure 1c. The application of ^{13}C CPMAS NMR under TPPM decoupling can effectively suppress the additional broadening attributed to heteronuclear dipolar interactions and thus leads to highly narrowed doublet signals for the ordered α_2 packing, whereas the α_1 spectrum

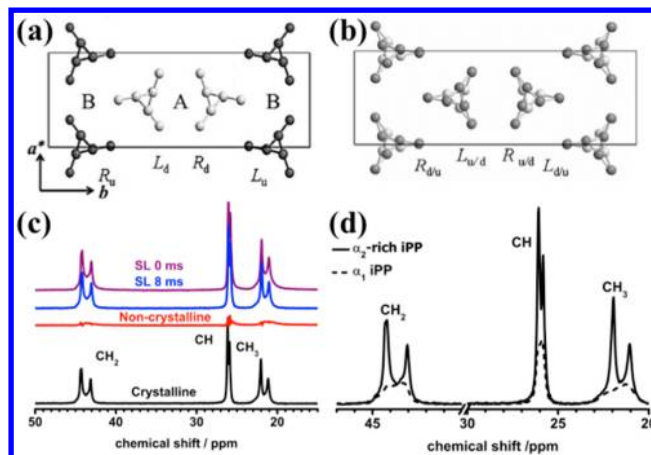


Figure 1. Unit-cell structures of (a) α_2 and (b) α_1 crystals.⁴² (c) ^{13}C CPMAS spectra of α_2 -rich iPP with (blue) and without (purple) a $T_{1\rho\text{H}}$ filter of 8 ms under a spin-locking field of 62.5 kHz and of pure amorphous (red) and pure crystalline (black) components obtained as linear combinations of the top two spectra. (d) Pure crystalline ^{13}C CPMAS NMR spectra of α_1 (dashed) and α_2 -rich (solid) iPP prepared via different annealing procedures.

remains broad with structureless features because of the structural disorder. The noncrystalline component in iPP is highly mobile at ambient temperatures ($T_g \sim 0$ °C) and thus gives low CP efficiency in the ^{13}C CPMAS NMR. The spin-locking filter of 8 ms effectively suppresses the noncrystalline signal. Finally, linear combinations of the filtered spectrum and the unfiltered spectrum yield the pure noncrystalline (red) and pure crystalline spectra (black) presented in Figure 1c. More detailed procedures are available in our previous work.^{47,48} The same procedure was applied to all ^{13}C CPMAS NMR spectra of the samples used in this study to obtain the pure crystalline spectra. The pure crystalline spectra of the original α_1 and α_2 -rich samples prepared via quiescent annealing are shown as dashed and solid lines, respectively, in Figure 1d. Among the three functional groups, the CH_2 peak exhibits the best contrast between the α_2 and α_1 line shapes. Thus, the CH_2 signals were used for the determination of the α_2 fraction (f_{α_2}). Based on the peak separation and line-shape fitting using a Gaussian line shape, the f_{α_2} for the original α_2 -rich sample was determined to be 0.53.

3.2. Chain-Packing Structure under Hot Drawing.

Figure 2 presents a typical engineering stress–strain curve of the original α_2 -rich sample drawn at 150 °C up to $\epsilon = 20.1$,

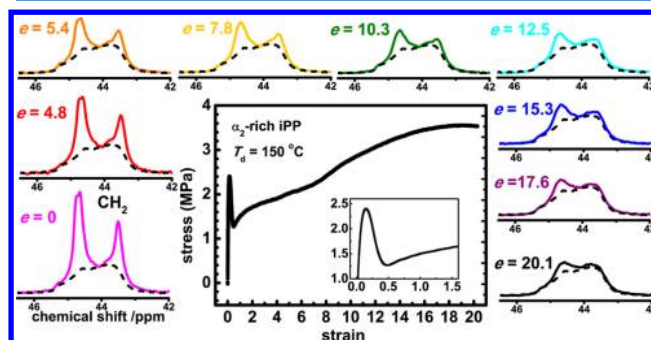


Figure 2. Stress–strain curve of the original α_2 -rich iPP drawn at 150 °C and the corresponding pure crystalline ^{13}C CPMAS spectra at various ϵ values.

where the yield point can be clearly observed at $e = 0.14$. After the yield point, the stress drops rapidly and then subsequently increases with increasing strain. The stress–strain curve finally levels off at $e > 18$, which may be attributed to a slight slippage of the sample from its clamps at such high strain. The ^{13}C CPMAS spectra of the CH_2 signals for the pure crystalline components at various e values are also shown in Figure 2. As a reference, the ^{13}C line shapes of the pure α_1 crystals are also inserted as dashed lines. The NMR spectra were measured after removing the sample from the Instron unit at the corresponding e values. At $e = 0$, the ^{13}C CH_2 and CH_3 signals confirm the presence of α_2 -rich structures and yield $f_{\alpha 2} = 0.53$. At $e = 4.8$, the CH_2 and CH_3 doublet peak heights decrease slightly compared to the doublet peak heights at $e = 0$, and the corresponding $f_{\alpha 2}$ is 0.46. The doublet signals decrease continuously with further increases in e . At $e = 20.1$, the doublet signals of each carbon are only a small portion of the total signal and imply $f_{\alpha 2} = 0.1$. The observed changes in the series of ^{13}C CPMAS spectra indicate that the α_2 structure continuously transformed into the α_1 structure under uniaxial drawing at $T_d = 150$ °C.

Meanwhile, similar $\alpha_2 \rightarrow \alpha_1$ transformations were also observed at $T_d = 100$ and 125 °C. Figure 3 presents the ^{13}C

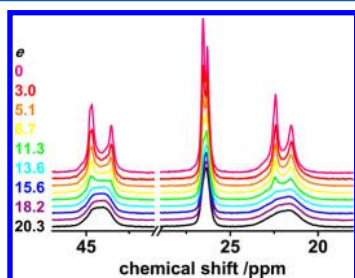


Figure 3. Pure crystalline ^{13}C CPMAS spectra of the original α_2 -rich iPP drawn at $T_d = 100$ °C at various e values.

CPMAS NMR spectra of the original α_2 -rich iPP drawn at $T_d = 100$ °C for various e values. The α_2 signals decrease rapidly with increasing e and disappear completely at $e = 13.6$ ($f_{\alpha 2} = 0$). Similar results were obtained at $T_d = 125$ °C (see Figure S1).

Drawing experiments were also conducted using the original α_1 iPP samples at various T_d s of 100, 125, and 140 °C. The α_1 sample had an onset T_m of 151 °C and a maximum T_m of 164 °C (Figure 11b). We therefore set the highest T_d at 140 °C to avoid any melting of the α_1 bulk crystals caused by annealing alone. The ^{13}C CPMAS NMR spectra of the original α_1 iPP drawn at 100 °C are depicted in Figure 4. The line shape is invariant over the entire e range, which confirms that the packing structure did not change during drawing at 100 °C ($f_{\alpha 2}$

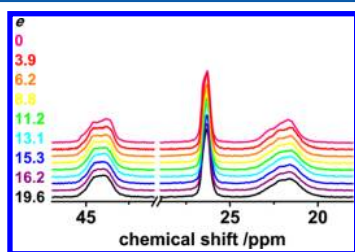


Figure 4. Pure crystalline ^{13}C CPMAS spectra of the original α_1 iPP drawn at $T_d = 100$ °C at various e values.

$= 0$). The same results were obtained at $T_d = 125$ °C (data are not shown).

Figure 5 shows the engineering stress–strain curve of the original α_1 sample at $T_d = 140$ °C and the corresponding ^{13}C

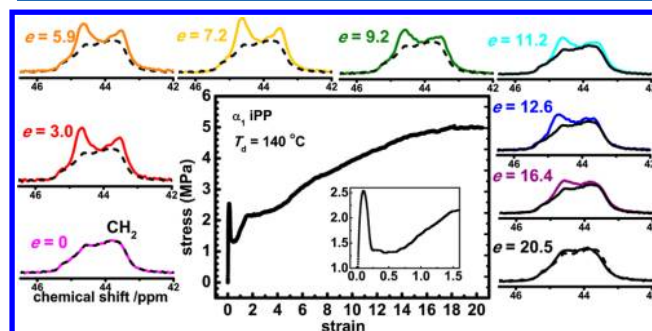


Figure 5. Stress–strain curve of the original α_1 iPP drawn at 140 °C and corresponding pure crystalline ^{13}C CPMAS spectra at various e values.

CPMAS NMR spectra at various e values. At $e = 3.0, 5.9$, and 7.2 , part of the α_1 structure can be clearly observed to change into the α_2 structure (e.g., $f_{\alpha 2} = 0.28$ at $e = 3.0$). The signals of the newly formed α_2 then gradually decrease with further increase in e . The structural evolution of the packing structure in the late stage of the process ($e > 7.2$) was very similar to the change in the original α_2 -rich iPP drawn at 150 °C. The experimental results indicate that the drawing of the α_1 sample at 140 °C involved two different transformation processes at the packing level.

Figure 6a shows the α_2 fractions of the original α_2 -rich iPP at $T_d = 100, 125$, and 150 °C as a function of e . The parameter $f_{\alpha 2}$ monotonically decreased with increasing e , and eventually, the

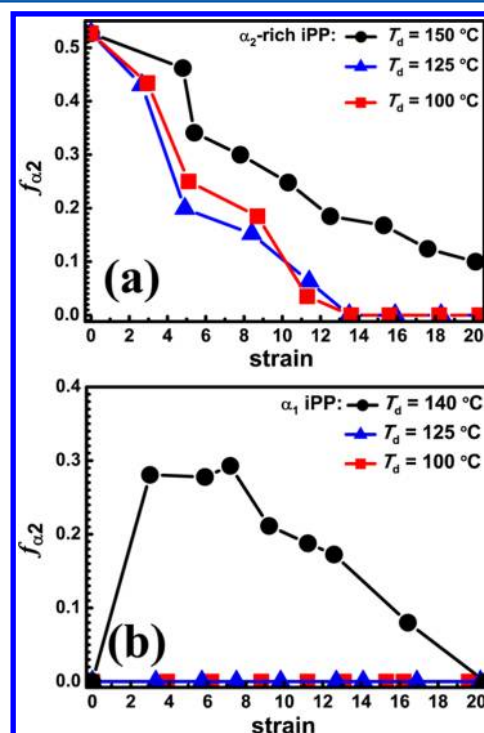


Figure 6. The e dependence of the $f_{\alpha 2}$ of (a) the original α_2 -rich iPP drawn at 100 (■), 125 (▲), and 150 °C (●) and (b) the original α_1 iPP drawn at 100 (■), 125 (▲), and 140 °C (●).

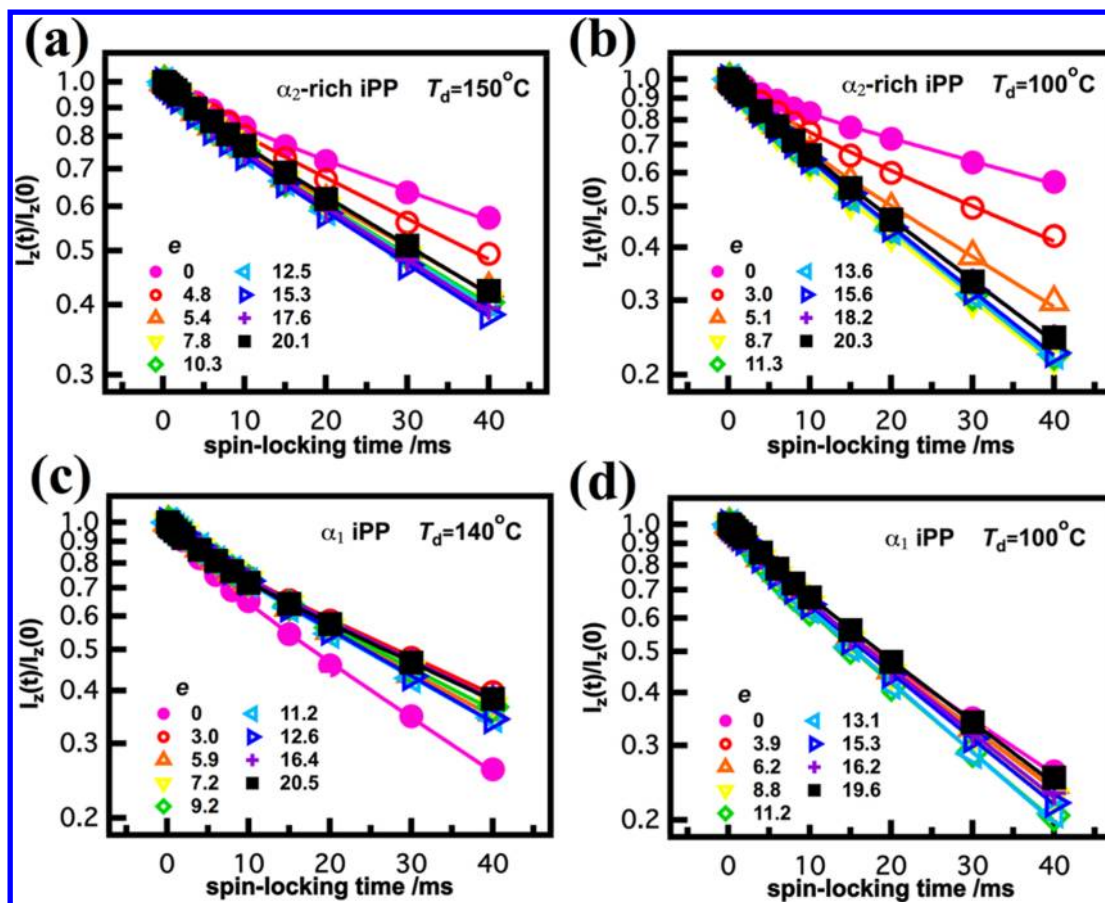


Figure 7. $T_{1\rho H}$ decay curves of the original α_2 -rich samples drawn at (a) 150 and (b) 100 °C and the original α_1 drawn at (c) 140 and (d) 100 °C at various e values.

original α_2 -rich crystals transformed into α_1 -dominant crystals at all T_d s. The transformation behavior was strongly dependent on T_d . The two curves at $T_d = 100$ and 125 °C are nearly identical, whereas the slope of the curve at 150 °C is less steep than that of the other two curves. At $T_d = 100$ and 125 °C, the α_2 structure transformed completely into α_1 crystal at $e \approx 14$. On the other hand, a small $f_{\alpha 2}$ of 0.10 remained even at $e = 20.1$ at 150 °C.

According to the literature, both quiescent crystallization of iPP melt at $T_c \geq 135$ °C and annealing of α_1 crystals above 150–165 °C lead to the formation of α_2 -rich crystals.^{42,47,48} The value of $f_{\alpha 2}$ increases with increasing T_c and T_a . Our recent SS-NMR study has found that the maximum $f_{\alpha 2}$ ranges from 0.47 to 0.66 at $T_c = 155$ °C, depending on stereoregularity.⁴⁸ In the current hot-drawing experiments, however, $f_{\alpha 2}$ was found to decrease with increasing e at all T_d values, even at 150 °C, indicating that the drawing process plays an essential role in the destruction of the original ordered crystals and induces newly formed disordered structures.

For the original α_1 sample, the values of $f_{\alpha 2}$ as a function of the e value at $T_d = 100$, 125, and 140 °C are plotted in Figure 6b. At 100 and 125 °C, the α_2 fraction remained invariant over the entire deformation range. At $T_d = 140$ °C, the value of $f_{\alpha 2}$ suddenly jumped to 0.28 at $e = 3.0$ and then remained nearly invariant up to $e = 7.2$. The $f_{\alpha 2}$ value then began to gradually decrease with further increase in e . These results clearly indicate that two different processes, one at $e < 7.2$ and one at $e > 7.2$, were at work in the structural changes at the packing level that arose under drawing at 140 °C. The observed $\alpha_1 \rightarrow \alpha_2$ change

under stretching in the initial stage is similar to the result of the quiescent annealing of the α_1 sample above 150 °C.⁴⁷ Thus, it might have been a simple annealing effect that caused this $\alpha_1 \rightarrow \alpha_2$ structural change at $T_d = 140$ °C. To evaluate this potential annealing effect, undrawn α_1 samples were left in the Instron chamber at 140 °C for 40 min, corresponding to the drawing time up to $e = 20$. However, no detectable α_2 fraction could be found in the α_1 samples that were annealed in this manner. We therefore reasonably conclude that the $\alpha_1 \rightarrow \alpha_2$ transformation observed at $e = 3.0$ at $T_d = 140$ °C is a unique structural change induced by hot drawing. It should be noted that our α_1 iPP samples did not transform into α_2 until $T_a \geq 162$ °C in the quiescent-annealing experiment.

3.3. $T_{1\rho H}$ under Hot Drawing. $T_{1\rho H}$ values are influenced by molecular dynamics in the frequency of several 10 kHz and by the phase structures of the various components and their sizes.⁴⁷ Simple relaxation measurements can detect structural changes in iPP under deformation. Figures 7a–d depict the $T_{1\rho H}$ decay curves of the original α_2 -rich samples drawn at 150 and 100 °C and of the original α_1 samples at 140 and 100 °C, respectively. The curves were obtained using the peak-top intensity for the highest ^{13}C CH peak. All decay curves exhibit approximately double exponential behavior and were therefore fitted with double exponential functions. For all samples, the $T_{1\rho H}$ values of the amorphous components were 5 ± 2 ms, and the $T_{1\rho H}$ values of the crystalline components spanned a wide range between 26 and 81 ms, depending on the original crystalline structure, T_d , and the e value. The best-fit $T_{1\rho H}$ values of the crystalline components are depicted in Figure 8 as

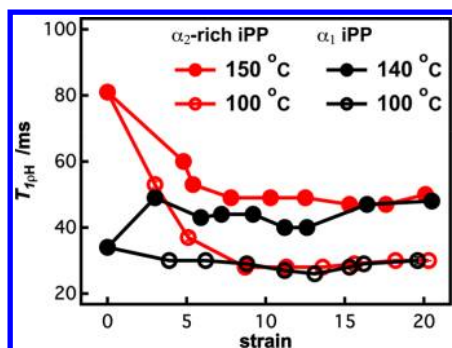


Figure 8. The ϵ dependence of the $T_{1\rho H}$ values for the original α_2 -rich samples drawn at 150 (red filled circles) and 100 °C (red open circles) and the original α_1 samples drawn at 140 (black filled circles) and 100 °C (black open circles).

a function of ϵ . In Figure 7a, at $T_d = 150$ °C, for the original α_2 -rich crystal, the $T_{1\rho H}$ relaxation of the crystalline signal immediately became much more rapid at small ϵ . The data presented in Figure 8 demonstrate that under these conditions the $T_{1\rho H}$ value dropped considerably from 81 ± 2 ms at $\epsilon = 0$ to 49 ± 1 ms at $\epsilon = 7.8$ and then remained nearly constant with increasing ϵ (50 ± 1 ms at $\epsilon = 20.1$). The acceleration of the relaxation behavior was more significant at $T_d = 100$ °C. Figures 7b and 8 illustrate the large and continuous drop in the $T_{1\rho H}$ decay curves from $\epsilon = 0$ (81 ± 2 ms) to 8.7 (30 ms). Further increase in ϵ did not change the $T_{1\rho H}$ values. For the original α_1 sample, hot drawing at 140 °C exerted the opposite effect on the $T_{1\rho H}$ relaxation of the original α_1 crystal. In Figures 7c and

8, it is apparent that the relaxation slowed as the $T_{1\rho H}$ value increased from 34 ± 1 ms at $\epsilon = 0$ to 49 ± 1 ms at $\epsilon = 3.0$. The $T_{1\rho H}$ value then decreased to 40 ± 1 ms at $\epsilon = 12.6$ and finally became 48 ± 1 ms at $\epsilon = 20.5$. For the original α_1 sample at $T_d = 100$ °C, the $T_{1\rho H}$ decay curves at the various ϵ values are similar to each other. The $T_{1\rho H}$ value of the original α_1 crystal decreased slightly to 30 ± 1 ms at $\epsilon = 19.6$. Based on all these $T_{1\rho H}$ results, it appears that it is not the original $T_{1\rho H}$ values at $\epsilon = 0$ but the T_d values that determine the $T_{1\rho H}$ values of deformed iPP samples at large ϵ values.

3.4. Crystal Thickness under Hot Drawing. A ^{13}C -detected ^1H spin-diffusion experiment⁵⁰ was performed to estimate the crystal thickness of the drawn and the undrawn samples at 90 °C, where the ^{13}C CH amorphous and crystalline peaks are well separated from each other and the ^1H spin diffusion between the two phases can be observed. For the original α_1 sample, the slice data of the ^{13}C spin-diffusion spectra of the CH resonance at various t_{SD} values are shown on the left side of Figure 9a, and the corresponding spectral intensities are plotted as filled triangles in Figure 9b. Relaxation experiments without the T_2 filter were also conducted to calibrate the pure spin-diffusion effect. The slice data of the relaxation spectra are displayed on the right side in Figure 9a, and their intensities are indicated by the open inverted triangles in Figure 9b. In Figure 9a, the spin-diffusion slices depict the signal intensity of the CH crystalline peak increasing with increasing t_{SD} and then beginning to notably decrease at $t_{\text{SD}} = 640$ ms because of the ^1H T_1 relaxation (^1H $T_1 \cong 1.2$ s), whereas the reference data exhibit only the relaxation effect. The t_{SD} dependence of the pure spin diffusion was obtained by

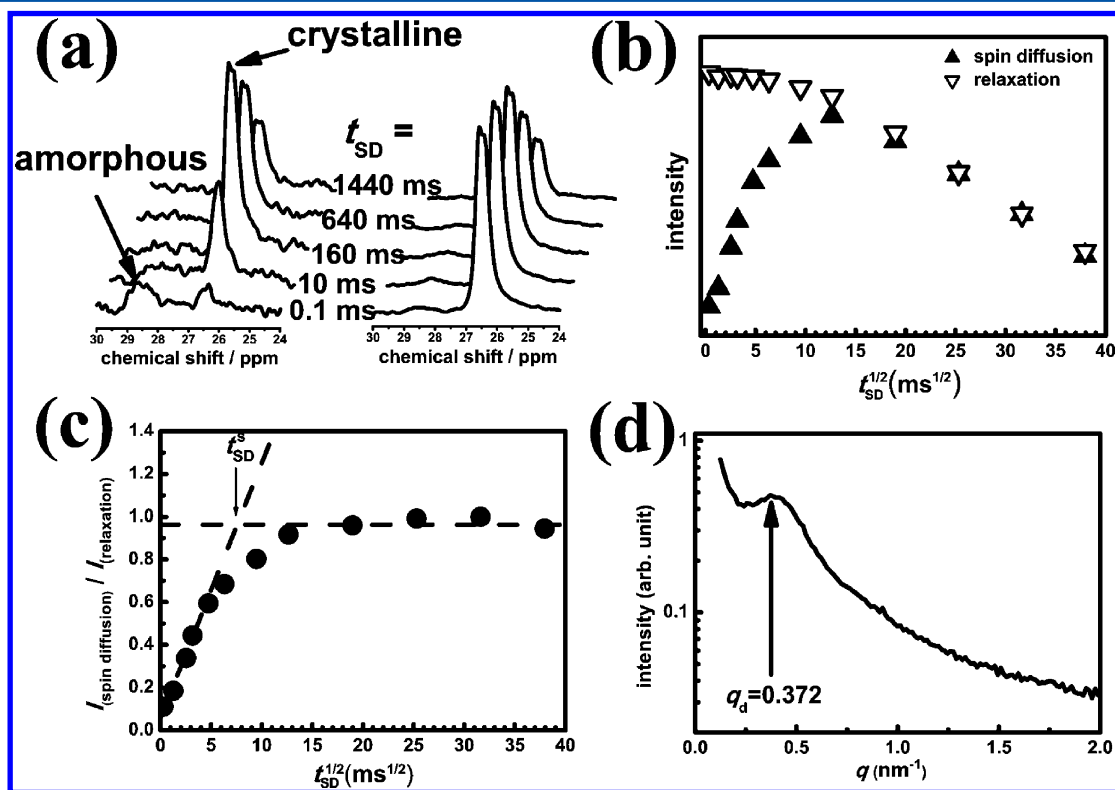


Figure 9. (a) Selected ^{13}C -detected ^1H spin diffusion (left) and relaxation (right) spectra of the CH signal of the original α_1 iPP for various t_{SD} s from 0.1 to 1440 ms at 90 °C. (b) The t_{SD} (filled triangles) and relaxation-time (open inverted triangles) dependence of the CH signal intensity in the crystalline regions. (c) The t_{SD} dependence of the corrected pure spin-diffusion intensity. (d) The SAXS data of the original α_1 iPP for the calibration of the spin-diffusion constant.

dividing the spin-diffusion intensities by the relaxation intensities in Figure 9b; the results are plotted in Figure 9c and indicate an initial linear buildup curve at $t_{SD}^{1/2} < 6 \text{ ms}^{1/2}$ and a plateau at $t_{SD}^{1/2} > 15 \text{ ms}^{1/2}$. A linear extrapolation of the initial region yields $(t_{SD}^s)^{1/2} = 7.59 \text{ ms}^{1/2}$ for the original α_1 sample, where t_{SD}^s denotes the value of the critical time for the spin diffusion to saturate in the crystalline domain.⁵⁰ Using the same method, we obtained a series of $(t_{SD}^s)^{1/2}$ values for the original and fully drawn samples listed in Table 1. Assuming a

Table 1. Crystal Thickness and Long Period of *i*PP Samples before and after Drawing Obtained from Spin-Diffusion Experiments at Room Temperature

sample	f_{cry}	$(t_{SD}^s)^{1/2}$ ($\text{ms}^{1/2}$)	crystal thickness (nm)	long period (nm)
α_2 -rich <i>i</i> PP, $e = 0$	0.66	8.9	14	22
α_2 -rich <i>i</i> PP, $e = 20.1$, T_d = 150 °C	0.82	6.9	20	26
α_1 <i>i</i> PP, $e = 0$	0.56	7.6	9	17
α_1 <i>i</i> PP, $e = 20.5$, T_d = 140 °C	0.77	7.1	17	23

two-phase model, the domain size of the two components can be estimated from the $(t_{SD}^s)^{1/2}$ value and the following equations:⁵⁰

$$d_{\text{cry(am)}} = \frac{\varepsilon}{f_{\text{am(cry)}}} \sqrt{4D_{\text{eff}} t_{SD}^s / \pi} \quad (1)$$

and

$$\sqrt{D_{\text{eff}}} := \frac{2\sqrt{D_{\text{cry}}D_{\text{am}}}}{\sqrt{D_{\text{cry}}} + \sqrt{D_{\text{am}}}} \quad (2)$$

where d_{cry} and d_{am} denote the crystalline and amorphous thicknesses, respectively, and ε denotes the dimensionality of the spin-diffusion process and is equal to 1 for the original lamellar structure. For deformed samples (fibrous structure), $\varepsilon = 1$,^{51,52} 2,²⁴ and 3⁵³ have been used to determine the crystalline thicknesses in PE, *i*PP, and Nylons, respectively. In this work, we simply applied $\varepsilon = 1$ for the largely deformed *i*PP samples. The parameters f_{cry} and f_{am} are the volume fractions of the crystalline and amorphous components, respectively. The parameter f_{cry} is obtained by the conversion of the wt % crystallinity determined via DPMAS NMR (section 3.6) using the reported densities.⁵⁴ D_{eff} is the effective spin-diffusion constant between the amorphous and the crystalline domains. The estimation of crystal thickness via NMR is highly dependent on the D_{eff} value. In this study, D_{eff} was calibrated using SAXS data.⁵⁰ Figure 9d shows the SAXS profile of the original α_1 *i*PP sample at ambient temperature, which indicates a scattering peak at $q = 0.372 \text{ nm}^{-1}$ and thus a long period of 16.9 nm. A lamellar thickness of 9.2 nm was estimated from the long-period value and the vol % crystallinity. Based on the SAXS result for the original α_1 sample, D_{eff} was determined to be $0.23 \text{ nm}^2/\text{ms}$. The diffusion constant in the crystalline region (D_{cry}) for *i*PP has been reported to be $0.7 \text{ nm}^2/\text{ms}$.⁵⁵ Using D_{eff} and D_{cry} , we obtained the diffusion constant in the amorphous region: $D_{\text{am}} = 0.11 \text{ nm}^2/\text{ms}$ at 90 °C for an MAS frequency of 4 kHz. Actually, molecular mobility of the amorphous region becomes restricted after drawing. D_{am} of largely deformed sample would increase compared with undrawn sample.²⁴ In our analysis, we did not consider change

in D_{am} and used the same $D_{\text{eff}} = 0.23 \text{ nm}^2/\text{ms}$ in highly deformed sample. Using the respective t_{SD} values and the vol % crystallinity for each sample, the crystal thicknesses and the long periods of the original and fully drawn samples ($e \approx 20$) were obtained; the results are listed in Table 1. For the α_2 -rich *i*PP, the initial crystal thickness was 14.1 nm. Hot drawing to $e = 20.1$ at 150 °C resulted in a crystal thickness of 20.1 nm. For the α_1 *i*PP, drawing at 140 °C nearly doubled the original crystal thickness of 9.2 to 17.0 nm at $e = 20.5$.

3.5. Molecular Dynamics under Hot Drawing. The molecular dynamics of the original α_2 -rich *i*PP and the original α_1 *i*PP before and after drawing to an e of approximately 20 at $T_d = 150$ and 140 °C, respectively, was investigated using CODEX NMR.³⁷ In the case of *i*PP stems, 3_1 helical stems perform discrete 3-site jump motions by 120° rotations around the helical axes and translations by one repeating unit at temperatures above 87 °C.³³ Figure 10a depicts the CODEX exchange (S) and reference (S_0) spectra of the undrawn α_2 -rich *i*PP for $t_m = 100 \text{ ms}$ and an evolution time of 2 ms at 120 °C. The signal intensities of all functional groups in the exchange spectrum at $t_m = 100 \text{ ms}$ were much smaller than the signal

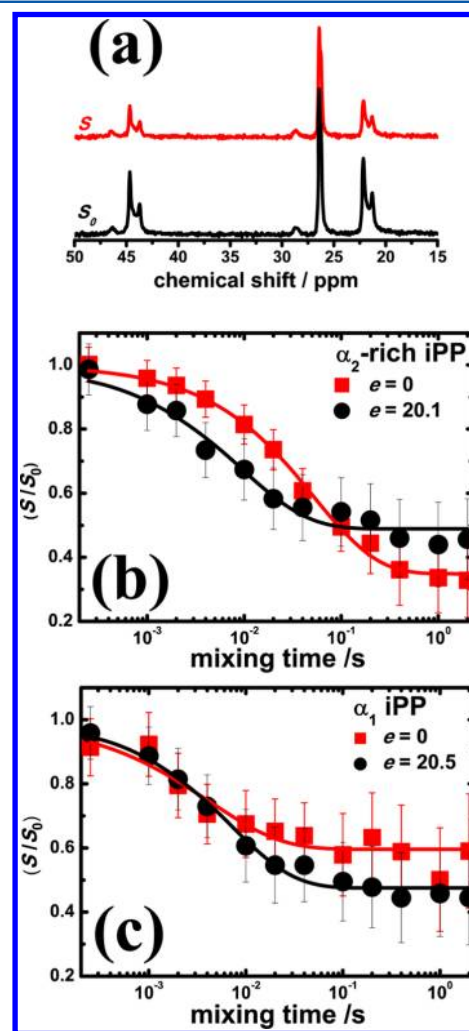


Figure 10. (a) CODEX exchange (S) and reference (S_0) spectra for the original α_2 -rich sample at $e = 0$ and $t_m = 100 \text{ ms}$ at 120 °C. CODEX t_m dependence of (S/S_0) intensity ratios of the CH_2 signals of (b) the original α_2 -rich *i*PP and (c) the original α_1 *i*PP at $e = 0$ (■) and $e \approx 20$ (●).

intensities in the reference spectrum, which is the evidence for helical jump motion.^{47,48} Figures 10b and 10c present the CODEX t_m dependence of the (S/S_0) intensity ratios of the CH₂ signal of the original α_2 -rich and α_1 iPP samples, respectively, at $e = 0$ (■) and $e \approx 20$ (●). The solid lines represent the best fits to the experimental results using the following empirical equation:³⁷

$$(S/S_0(t_m)) = 1 - a(1 - \exp(-(t_m/\langle\tau_c\rangle)^\beta)) \quad (3)$$

where a is related to the number of dynamically accessible sites, p , as follows: $a = (p - 1)/p$. The 3₁ helices of iPP render three sites accessible and thus yield a theoretical a value of 0.667. The parameter $\langle\tau_c\rangle$ is the correlation time of helical jump motion. The drawing exponent β ($0 \leq \beta \leq 1$) simply represents the distribution of the correlation times. The expression $\beta = 1$ corresponds to a single correlation time, and a smaller β value provides a wider distribution of correlation times.

The best-fit parameters of the a , $\langle\tau_c\rangle$, and β values of four samples are listed in Table 2. The $\langle\tau_c\rangle$ values of the original α_2 -

Table 2. Best-Fit CODEX Parameters of the iPP Samples before and after Drawing, Obtained at 120 °C

sample	a	$\langle\tau_c\rangle$ (ms)	β
α_2 -rich iPP, $e = 0$	0.65 ± 0.02	52.5 ± 5.2	0.67 ± 0.03
α_2 -rich iPP, $e = 20.1$, $T_d = 150$ °C	0.51 ± 0.02	9.3 ± 1.8	0.63 ± 0.08
α_1 iPP, $e = 0$	0.40 ± 0.02	4.2 ± 1.3	0.59 ± 0.13
α_1 iPP, $e = 20.5$, $T_d = 140$ °C	0.52 ± 0.01	7.1 ± 0.9	0.67 ± 0.06

rich and α_1 iPP at $e = 0$ are 52.4 ± 5.2 and 4.2 ± 1.3 ms, respectively, indicating that the molecular dynamics in the former was 12-fold slower than that in the latter. After deformation, the $\langle\tau_c\rangle$ of the original α_2 -rich iPP decreased significantly to 9.3 ± 1.8 ms, indicating an unexpectedly much more rapid helical jump motion in the largely deformed iPP crystals. The $\langle\tau_c\rangle$ of the original α_1 sample increased slightly from 4.2 ± 1.3 to 7.1 ± 0.9 ms at $e = 20.5$ at 140 °C. The a value of 0.65 ± 0.02 for the original α_2 -rich iPP is quite consistent with the theoretical expectation. However, the a values for the undrawn and drawn α_1 samples and the drawn α_2 -rich samples are much smaller than the theoretical a values. These reductions in a value are attributed not to a change in the number of available sites but to an additional loss of correlation in the evolution time.⁴⁸ The $\langle\tau_c\rangle$ of 4–7 ms that was obtained is close to the limit of the slow dynamic range and comparable to the evolution time of 2.0 ms. The correlation loss during the evolution period can therefore no longer be ignored in the slow-dynamics limit. Such an effect leads to an additional reduction in the a value. However, the additional loss of correlation does not influence the $\langle\tau_c\rangle$ values in the vicinity of the slow-dynamics limit. For all samples, $\beta \neq 1$, indicating heterogeneity in the molecular dynamics. Considering the experimental errors, the β values before and after drawing are similar for both the original α_2 -rich samples and the original α_1 samples.

The long time of CODEX experiments at high temperature (31 h) might influence molecular dynamics of highly drawn iPP. We further investigated annealing effects on molecular dynamics of the undrawn and drawn iPP samples. Single- t_{mix} CODEX experiments which only required 1.5 h were further performed on both undrawn and drawn samples before and after annealing at 120 °C for 30 h. For both undrawn and

drawn samples, the single- t_{mix} CODEX intensity ratios for the CH₂ signals before annealing are identical with those after annealing (Figures S3) as well as the series of CODEX data at the same t_{mix} in Figure 10. Therefore, it is concluded that not annealing but deformation leads to faster molecular dynamics of stems in the original α_2 -rich crystals.

3.6. Melting Temperature and Crystallinity. Figures 11a and 11b present the DSC heating curves of the original α_2 -rich

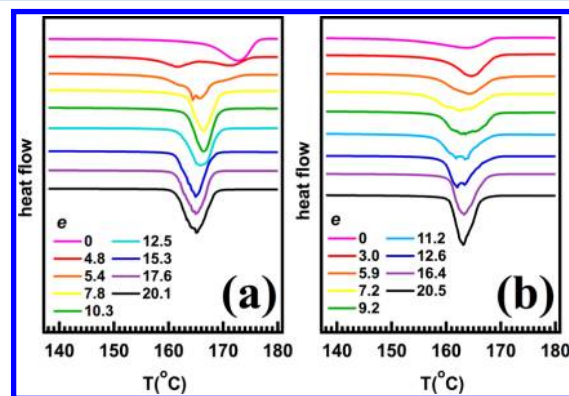


Figure 11. DSC curves of (a) the original α_2 -rich iPP drawn at 150 °C and (b) the original α_1 iPP drawn at 140 °C at various e values.

iPP drawn at 150 °C and the original α_1 iPP drawn at 140 °C, respectively, as a function of the e value. Before drawing, the α_2 -rich iPP had an initial melting temperature (T_m) of 172.7 °C. In Figure 11a, for the original α_2 -rich sample at $T_d = 150$ °C, the DSC curve at $e = 4.8$ exhibits clear double melting peaks with maxima at 161.3 and 171.4 °C. At $e = 5.4$, the double melting peaks begin to overlap with each other and then completely merge at $e = 7.8$. At $e = 20.1$, a single sharp melting peak is observed at 165.0 °C, which is 7.7 °C lower than the initial T_m . Figure 11b shows that the original α_1 iPP had a very broad initial endothermic peak at $T_m = 163.6$ °C. Drawing slightly increased the T_m to 164.6 °C at $e = 3.0$, and further drawing led to broadening of the endothermic peak up to $e = 9.2$, followed by subsequent narrowing. At $e = 20.5$, the α_1 iPP heating curve exhibits a sharp peak at 163.1 °C, close to the initial value. In contrast to the original α_2 -rich iPP drawn at 150 °C, the original α_1 iPP drawn at $T_d = 140$ °C did not exhibit double melting behavior.

DSC measurement, a well-known method of determining the crystallinity of semicrystalline polymers, relies on the value of ΔH for the 100% crystalline form. However, the ΔH values that have been reported for 100% α -crystalline iPP range between 137 and 221 kJ/mol.⁵⁴ The melting and recrystallization process during heating also influences the apparent crystallinity. Investigating the ¹³C DPMAS NMR spectrum at high temperatures below T_m is another method of determining the crystallinity of iPP because the ¹³C chemical shifts of the crystalline and amorphous signals are well separated from each other at such temperatures. Figures 12a and 12b present the ¹³C DPMAS NMR spectra (black lines) of the original α_2 -rich sample for $e = 0$ and 20.1 at $T_d = 150$ °C and the original α_1 iPP for $e = 0$ and 20.5 at $T_d = 140$ °C, respectively. At 90 °C, the CH and CH₂ crystalline signals were observed to be separate from the signals of the amorphous structures. The CH signals were better separated than the CH₂ signals. Thus, peak fitting using a Lorentzian line shape was applied to the CH peaks to determine the crystallinities. The best-fit curves of the

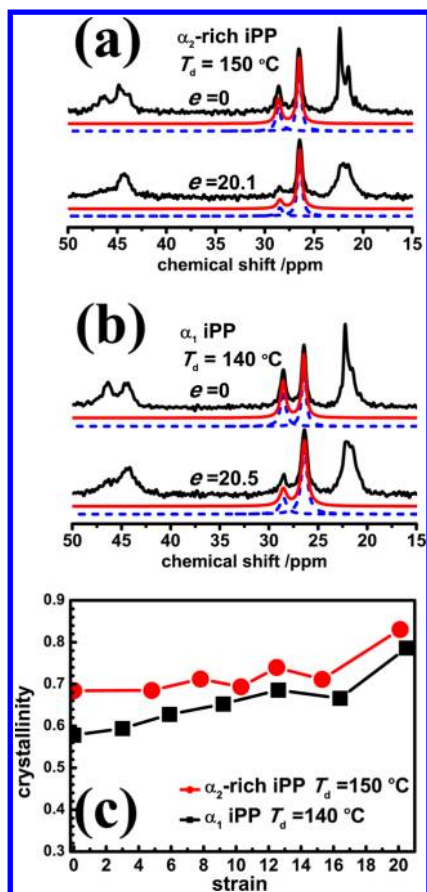


Figure 12. Experimental (black line) and calculated (blue and red lines) ^{13}C DPMAS NMR spectra of the CH regions at 90°C for (a) the original α_2 -rich iPP drawn at 150°C at $e = 0$ and 20.1 and (b) the original α_1 iPP drawn at 140°C at $e = 0$ and 20.5. (c) e dependence of the crystallinity of the original α_2 -rich iPP drawn at $T_d = 150^\circ\text{C}$ (●) and the original α_1 iPP drawn at 140°C (■).

individual peaks (blue) and the peak sums (red) are included in Figures 12a,b. At $e = 0$, the original α_2 -rich and α_1 samples exhibited crystallinities of 68 and 58%, respectively. Figure 12c depicts the e dependence of the crystallinity of the original α_2 -rich samples (filled red circles) and the original α_1 samples (filled squares). The crystallinities of both the original α_2 -rich samples and the original α_1 samples increase monotonically with increasing e because of strain-induced crystallization. When e reached approximately 20, the crystallinities of the former and the latter increased to 83 and 79%, respectively.

The CH_3 group displays overlapped amorphous and crystalline signals in Figures 12a,b. For the original α_2 -rich sample, a sharp doublet line shape can be observed at $e = 0$, and this sharp doublet line shape becomes a broad and structureless peak at $e = 20.1$. Two structures contribute to the initial sharp signals. One structure is the α_2 structure, and the other structure is the highly mobile amorphous signal. For the α_1 sample, the spectrum of the undrawn sample exhibits overlapped CH_3 peaks of sharp and broad signals, whereas the spectrum of the drawn sample contains only a broad component. The sharp peak in the undrawn α_1 spectrum is simply assigned to the highly mobile amorphous component. The absence of sharp CH_3 signals in the two fully drawn spectra indicates that the molecular dynamics of the amorphous regions is constrained because of the large deformation. This observation is consistent with the retardation of the amorphous

dynamics observed by Litvinov et al. via the ^1H T_2 values of highly deformed iPP samples.²⁴

4. DISCUSSION

4.1. Two Crystal Transformations under Hot Drawing.

Structural evolutions of semicrystalline polymers have been explained in terms of three-stage models and/or melting and recrystallization based on different experimental techniques and conditions, including T_d and e .^{1–23} In this study, packing structure was used as a structural probe to study the mechanism of deformation. Of the structures that are detectable under deformation, the packing structure is the structure with the shortest length scale. From the conformational point of view, the observed change in packing structure from α_1 to α_2 (or α_2 to α_1) requires changes in the orientations of the CH_3 groups without any change in the original handedness. This process requires 180° rotation of the entire chain around its normal axis to reverse itself, which is very difficult in the limited space available in solid crystals. Therefore, the $\alpha_1 \rightarrow \alpha_2$ transformation induced by annealing at 150 – 165°C has been attributed to melting and recrystallization.^{43,44} The same logic would hold for $\alpha_1 \rightarrow \alpha_2$ transformation and vice versa under hot drawing. In these two processes, the three-stage model, in which the local packing structure should be preserved, can naturally be excluded.

For the original α_1 sample, the sudden increase in f_{a2} within a small strain range ($e = 3.0$ – 7.2) at $T_d = 140^\circ\text{C}$ (Figure 6b) is assigned to the isotropic melting and recrystallization induced by stress. The external field, which behaves as a destructive force for rigid crystals, and the latent heat released by necking^{56,57} lower the temperature required (162°C for our original α_1 sample) for local melting and recrystallization to occur in a quiescent environment. The stress–strain curve levels off at $e = 1.7$ (Figure 5), which seems to be a second yielding point that has been interpreted in terms of melting and recrystallization.^{58,59} The sudden increase in the apparent $T_{1\rho\text{H}}$ value from 34 ms at $e = 0$ to 49 ms at a small e value of 3.0 at $T_d = 140^\circ\text{C}$, as shown in Figure 8, also supports the hypothesis of melting and recrystallization. Within a similar e range of 5–9, Sadler and Barham have similarly proven that local melting occurs via the isotopic segregation of PE/DPE blends using NS. They have determined that the segregation region is larger than the size of a single molecule (radius of gyration, $R_g \approx 130$ – 300 Å).¹⁴ They have also confirmed such segregations do not occur in the late process after necking using a series of NS experiments.^{15,16}

The reverse $\alpha_2 \rightarrow \alpha_1$ transformations in the original α_2 -rich crystals and the recrystallized α_2 crystals in the original α_1 sample in the later stage of drawing ($e \geq 7.2$) provide important information for the understanding of major deformations. Unlike the sudden $\alpha_1 \rightarrow \alpha_2$ transformation in the early stage ($e = 3.0$ – 7.2) at 140°C , the $\alpha_2 \rightarrow \alpha_1$ transformation is a continuous process throughout the entire deformation range at all T_d s. The mechanism therefore must be different from the isotropic melting and recrystallization induced by stress. As demonstrated in the current study and by previous efforts,^{33,47,48} the stems of iPP perform 120° helical jump motions in the crystalline regions at all T_d s. Upon hot drawing, chains should cooperatively diffuse between the crystalline and amorphous regions. Such motion leads to the unfolding of folded chains (melting) as the e value increases. The melted chains maintain their oriented states under external force and immediately recrystallize into new crystals. This newly found

process is named as molecular-level directional melting and recrystallization induced by chain diffusion. The scale of the melting and recrystallization driven by chain diffusions should be much smaller than the scale of the isotropic melting and recrystallization induced by stress.

Another interesting feature is the T_d dependence of the $\alpha_2 \rightarrow \alpha_1$ transformation in the original α_2 -rich sample (Figure 6a). There are several possible explanations for the observed T_d dependence. The $\alpha_2 \rightarrow \alpha_1$ transformation is driven by two processes: melting and recrystallization. The melting process is related to chain diffusions, which are induced by successive helical jump motions along one preferential direction. If the local helical jumps do not exhibit any preference in moving direction under stress, two successive helical jumps can cancel out individual translations along the chain direction and do not induce the effective destruction of the original crystals under deformation. Meanwhile, the recrystallization is dominated by the kinetics of crystallization. In quiescent crystallization, a lower T_c kinetically prefers the formation of α_1 crystals. If the same tendency can be applied to recrystallization under stress, a lower T_d should lead to a higher α_1 fraction. Thus, two processes, melting induced by chain diffusion and recrystallization induced by kinetics, drive the apparent $\alpha_2 \rightarrow \alpha_1$ transformation. Another reason is the effect of isotropic melting and recrystallization, which was observed in the original α_1 sample within a small ϵ range at $T_d = 140$ °C (Figure 6b). This process may also have contributed during the deformation of the original α_2 -rich samples at $T_d \geq 140$ °C, slowing the apparent $\alpha_2 \rightarrow \alpha_1$ transformation.

Very recently, Hong et al. have proposed a novel strategy of ^{13}C – ^{13}C double quantum (DQ) NMR combined with ^{13}C selective isotope labeling that can precisely characterize chain-folding structures.⁶⁰ To confirm the unfolding process induced by chain diffusions and extended/folded crystals under major deformation, it is necessary to directly observe the evolution of unfolded structures from the original folded chains under deformation. At present, we are investigating the unfolding process of drawn ^{13}C -labeled *i*PP samples using ^{13}C – ^{13}C DQ NMR. The results will be reported elsewhere.

Finally, we would like to mention the fragmentation of the original lamellae during the initial stage of deformation. The large drop in the $T_{1\rho\text{H}}$ values for the original α_2 -rich samples within a small ϵ range, is shown in Figure 8. The lower T_d leads to steeper decays of the $T_{1\rho\text{H}}$ values. The observed changes in the $T_{1\rho\text{H}}$ values could be attributed to the fragmentation of the crystals, as reported in the literature,⁶ and/or the $\alpha_2 \rightarrow \alpha_1$ transformation. Fragmentations lead to smaller crystal sizes along the crystallographic a and b axes. Thus, the sizes of the fragments would influence the spin-diffusion process between the amorphous and crystalline regions, leading to decreasing in the $T_{1\rho\text{H}}$ values. Moreover, α_2 and α_1 crystals have different $T_{1\rho\text{H}}$ values because of the differences in their packing structures and the sizes of individual crystals.⁴⁸ Thus, the transformation from α_2 to α_1 via chain diffusions would also lead to a reduction in the $T_{1\rho\text{H}}$ value. For the original α_1 sample, the deformation at $T_d = 100$ °C was not accompanied by a large change in the $T_{1\rho\text{H}}$ value; the absence of a large change can be simply attributed to the thin lamellae in the original α_1 samples. In this case, the fragmentation of the lamellae did not influence the spin-diffusion path between the amorphous and crystalline regions.

4.2. Crystalline Structures vs Large-Amplitude Dynamics. Recently, Miyoshi et al. reported that the helical jump

rate of stems in α_1 *i*PP crystals prepared at low T_c is 32-fold higher than the helical jump rate of stems in α_2 -rich crystals prepared at high T_c and have suggested that both the thickness of the lamellae and the packing structure influence the molecular dynamics of the crystalline stems.⁴⁷ Thicker lamellae imply greater lengths of the stems that participate in the helical jumps. Such an effect would naturally restrict the molecular dynamics. With regard to packing effects, Cheng et al. have observed the contraction of the crystal unit cell in α -form *i*PP by 0.1 Å along both the a and b crystallographic axes with the supercooling temperature decreasing from 100 to 20 °C.⁶¹ Naiki et al. have also observed a similar contraction during annealing at high temperature and have correlated this contraction with the $\alpha_1 \rightarrow \alpha_2$ transformation.⁴⁴ Slightly denser packing of the *i*PP chains in the ab plane of a α_2 -rich crystal is also a possible cause of restriction of the helical jump motions of the *i*PP chains. However, because an increase in T_c or T_a causes a simultaneous increase both in the thickness of the lamellae and in f_{α_2} , it is difficult to separate the effect of the crystal thickness on the molecular dynamics from the effect of the packing structure in quiescent experiments.

Under hot drawing, the packing structure of the original α_1 *i*PP drawn at 140 °C remained invariant, but the crystal thickness increased from 9.2 at $\epsilon = 0$ to 17.0 nm at $\epsilon = 20.5$. This large increase in the crystal thickness led to only a small increase in the $\langle\tau_c\rangle$ of the helical jumps, from 4.2 to 7.1 ms at 120 °C. The effect of the crystal thickness on the molecular dynamics of the drawn sample was very minor. In contrast, in the original α_2 -rich sample, the $\langle\tau_c\rangle$ value of 52.4 ms at $\epsilon = 0$ significantly decreased to 9.3 ms at $\epsilon = 20.1$, accompanied by an increase in the crystal thickness (14.1 \rightarrow 20.1 nm) and a decrease in the α_2 fraction (0.53 \rightarrow 0.10). These experimental results clearly indicate that the enhanced mobility of the stems can reasonably be explained in terms of the disordering of the chain-packing structures. The slightly denser packing of the *i*PP chains in a α_2 -rich crystal highly restricts the helical jump motions of the *i*PP stems. Thus, the packing structure influences the stem dynamics more significantly than does the crystal thickness.

According to the literatures,^{24,36,62} the molecular dynamics of amorphous, interfacial, and crystalline segments are generally restricted by the increased crystallinity, crystal thickness, and segmental orientation that occur under large deformation. The present study also confirms that the crystallinity (Figure 12c) and the crystal thickness (Table 1) increase with increasing ϵ during hot drawing. In addition, the restriction of the local amorphous regions was also detected via ^{13}C DPMAS (Figures 12a,b). Crystalline stem dynamics, however, becomes much more rapid with disordering of the packing structure, although the crystal thickness significantly increases. Thus, to establish the relation between the structure and the dynamics under deformation, careful investigations of structures at different length scales are necessary. The same discussion applies to the melting temperatures of deformed *i*PP samples (see next section).

4.3. Hierarchical Crystalline Structures vs Melting Behavior. The T_m of a semicrystalline polymer is dependent on the crystal thickness, as indicated by the Gibbs–Thomson equation ($T_m = T_m^0(1 - A/l_c)$),⁶³ where T_m^0 is the equilibrium melting temperature, A is a constant value, and l_c is the thickness of the lamellae. Increasing the thickness of the lamellae leads to a higher T_m . Yamada et al. have confirmed this effect of l_c on the T_m for α -form *i*PP.⁶⁴ As explained in the

previous section, an increase in T_c always causes an increase both in the crystal thickness and in f_{a2} in α -form iPP. Guerra et al. have also suggested a correlation between T_m and the packing order.⁴³ Similar to the discussion of the molecular dynamics, it is not clear how the crystal thickness and the packing structure influence the bulk T_m value.

Under hot drawing, the iPP samples investigated in the present study exhibited very complex melting behavior depending on the original structure and the value of e . Here, we interpret the present DSC results based on the fragmentation of the crystals,^{1,6} the crystal thickness, and f_{a2} and discuss the relation between T_m and structures. As shown in Figure 11, the original α_2 -rich sample exhibited $T_m = 173$ °C, whereas the original α_1 sample exhibited $T_m = 164$ °C. The high T_m of the former can be simply explained in terms of the thick lamellae (thickness = 14.1 nm) and the ordered packing ($f_{a2} = 0.53$), and the low T_m of the latter can be understood as the result of the crystal thickness of 9.2 nm and $f_{a2} = 0$. Under deformation, the lamellar structure of a α_1 iPP crystal changes to a blocky structure via rotations, sliding, and fragmentation ($e < \sim 7$), as confirmed by the sharp drop in the $T_{1\rho H}$ value observed in this study and in previous work.⁶ In contrast, for an initially α_2 -rich sample, part of α_2 transforms into α_1 structure. The fragmented α_1 and α_2 structures would be assigned to low and high melting temperatures, respectively, at $e = 4.8$ in Figure 11a. With a further increase in the e value, the two melting peaks merge into one. Under further deformation, the crystal thickness increases up to 20.1 nm in the fibrous state and the α_2 fraction continuously decreases to 0.1. The former and latter processes should exert opposite effects on T_m and lead to an increase and a decrease in T_m , respectively. At $e = 20.1$, despite the increased crystal thickness, the final α_1 -rich sample possessed a lower T_m (165 °C) than the undrawn α_2 -rich sample. It is therefore reasonable to conclude that the macroscopic T_m value of the drawn sample was more strongly influenced by the packing structure than by the crystal thickness. Similarly, for the original α_1 sample, the fragmentation and rotation of the lamellae occurred during the initial drawing stage, $e < \sim 7$. Melting of the unstable α_1 and recrystallization into the α_2 structure also occurred, as detected via ¹³C CPMAS NMR (Figure 5). These two competing effects—fragmentation of the crystals and the $\alpha_1 \rightarrow \alpha_2$ transformation—gave rise to a single T_m peak at 165 °C at $e = 3.0$ and the broadening of the melting peaks at $e = 5.9$ – 9.2 . Then, as the hot drawing proceeded, the crystal thickness increased, and the newly formed α_2 fraction began to decrease, similar to the original α_2 -rich crystals. Because of these two opposite effects, the melting temperature did not change in a wide range throughout the deformation process. The two different samples under hot drawing ultimately exhibited very similar T_m values at $e \approx 20$. Despite the different deformation pathways of the original α_1 and α_2 structures over a small e range, the final structures, dynamics, and thermal properties of the two different samples drawn to $e \approx 20$ at high T_d s were very similar because the final crystals were formed via the same mechanism of directional melting and recrystallization induced by chain diffusion.

Numerous studies concerning the hot drawing of iPP samples have been reported.^{6–10,19–21} However, there has been no systematic effort to investigate the relations among the structure, dynamics, and thermal properties of deformed iPP materials. As we demonstrated in this study, the packing order plays an important role in determining the stem dynamics and

thermal properties of drawn iPP. This finding indicates that further improvement of the thermal properties of processed iPP materials could be achieved by producing a highly ordered packing structure.

5. CONCLUSIONS

¹³C CPMAS NMR detected two reverse transformations ($\alpha_2 \rightarrow \alpha_1$ and $\alpha_1 \rightarrow \alpha_2$) in α -form iPP upon hot drawing, indicating two different melting and recrystallization processes at different length scales in different e ranges. The sudden increase in the α_2 fraction in the original α_2 at small e was assigned to the isotropic melting and recrystallization induced by stress. The continuous transformation from α_2 to α_1 over the entire deformation range was assigned to the molecular-level directional melting and recrystallization facilitated by chain diffusion. These transformations demonstrate that, except for the solid-phase transformation described by the three-stage model^{1–9} and the isotropic melting and recrystallization process,^{13,14,17} molecular-level directional melting and recrystallization attributable to chain diffusion also play an important role in the large deformation of iPP samples under hot drawing. Furthermore, the structural changes induced by chain diffusion lead to unexpected stem dynamics and thermal properties in processed iPP materials. Under large deformation, the resultant disordered packing structure results in more rapid molecular dynamics of the stems and a lower T_m , even though the crystal thickness increases under hot drawing. On the basis of these findings, we conclude that the local packing structure is a primary structural factor that governs both the stem dynamics and the T_m of iPP. The relation thus established among the local packing structure, the molecular dynamics, and the thermal properties will inform the production of iPP materials with improved thermal properties.

■ ASSOCIATED CONTENT

Supporting Information

¹³C CPMAS NMR spectra of the original α_2 -rich iPP drawn at $T_d = 125$ °C, DSC, and annealing effects on molecular dynamics. This material is available free of charge via the Internet at <http://pubs.acs.org>.

■ AUTHOR INFORMATION

Corresponding Author

*E-mail miyoshi@uakron.edu (T.M.).

Notes

The authors declare no competing financial interest.

■ ACKNOWLEDGMENTS

This work was financially supported by the National Science Foundation. (Grant DMR-1105829) and UA startup fund. The authors thank our department engineering technician Mr. Ed Laughlin for fabricating all the necessary parts for the hot-drawing experiments and Mr. Hao Liu for SAXS measurement.

■ REFERENCES

- (1) Peterlin, A. *J. Mater. Sci.* **1971**, *6*, 490–508.
- (2) Peterlin, A. *Colloid Polym. Sci.* **1987**, *265*, 357–382.
- (3) Petermann, J.; Kluge, W.; Gleiter, H. *J. Polym. Sci., Part B: Polym. Phys.* **1979**, *17*, 1043–1051.
- (4) Adams, W. W.; Yang, D.; Thomas, E. L. *J. Mater. Sci.* **1986**, *21*, 2239–2253.
- (5) Koike, Y.; Cakmak, M. *Macromolecules* **2004**, *37*, 2171–2181.

- (6) Nozue, Y.; Shinohara, Y.; Ogawa, Y.; Sakurai, T.; Hori, H.; Kasahara, T.; Yamaguchi, N.; Yagi, N.; Amemiya, Y. *Macromolecules* **2007**, *40*, 2036–2045.
- (7) Hong, Z.; Cong, Y.; Qi, Z.; Li, H.; Zhou, W.; Chen, W.; Wang, X.; Zhou, Y.; Li, L. *Polymer* **2012**, *53*, 640–647.
- (8) Ran, S.; Zong, X.; Fang, D.; Hsiao, B. S.; Chu, B.; Phillips, R. A. *Macromolecules* **2001**, *34*, 2569–2578.
- (9) Sakurai, T.; Nozue, Y.; Kasahara, T.; Mizunuma, K.; Yamaguchi, N.; Tashiro, K.; Amemiya, Y. *Polymer* **2005**, *46*, 8846–8858.
- (10) Zuo, F.; Keum, J. K.; Chen, X.; Hsiao, B. S.; Chen, H.; Lai, S.-Y.; Wevers, R.; Li, J. *Polymer* **2007**, *48*, 6867–6880.
- (11) Chuah, H. H.; Lin, R. S.; Porter, R. S. *Macromolecules* **1986**, *19*, 2732–2736.
- (12) Jiang, Z.; Tang, Y.; Rieger, J.; Enderle, H.-F.; Lilge, D.; Roth, S. V.; Gehrke, R.; Heckmann, W.; Men, Y. *Macromolecules* **2010**, *43*, 4727–4732.
- (13) Flory, P.; Yoon, D. *Nature* **1978**, *276*, 226–229.
- (14) Sadler, D. M.; Barham, P. J. *Polymer* **1990**, *31*, 36–42.
- (15) Sadler, D. M.; Barham, P. J. *Polymer* **1990**, *31*, 43–45.
- (16) Sadler, D. M.; Barham, P. J. *Polymer* **1990**, *31*, 46–50.
- (17) Wu, W.; Wignall, G. D.; Mandelkern, L. *Polymer* **1992**, *33*, 4137–4140.
- (18) Takayanagi, M.; Kajiyama, T. *J. Macromol. Sci. Phys., B* **1973**, *8*, 1–27.
- (19) De Rosa, C.; Auriemma, F. *J. Am. Chem. Soc.* **2006**, *128*, 11024–11025.
- (20) Ma, Z.; Shao, C.; Wang, X.; Zhao, B.; Li, X.; An, H.; Yan, T.; Li, Z.; Li, L. *Polymer* **2009**, *50*, 2706–2715.
- (21) Xu, W.; Martin, D. C.; Arruda, E. M. *Polymer* **2005**, *46*, 455–470.
- (22) Liu, Y.; Cui, K.; Tian, N.; Zhou, W.; Meng, L.; Li, L.; Ma, Z.; Wang, X. *Macromolecules* **2012**, *45*, 2764–2772.
- (23) Nakamura, K.; Aoike, T.; Usaka, K.; Kanamoto, T. *Macromolecules* **1999**, *32*, 4975–4982.
- (24) Hedesiu, C.; Demco, D. E.; Remerie, K.; Blu, B.; Litvinov, V. *Macromol. Chem. Phys.* **2008**, *209*, 734–745.
- (25) Hong, K.; Rastogi, A.; Strobl, G. *Macromolecules* **2004**, *37*, 10165–10173.
- (26) Yamada, K.; Kamezwa, M.; Takayanagi, M. *J. Appl. Polym. Sci.* **1981**, *26*, 49–60.
- (27) De Rosa, C.; Auriemma, F.; De Lucia, G.; Resconi, L. *Polymer* **2005**, *46*, 9461–9475.
- (28) Kanamoto, T.; Tsuruta, A.; Tanaka, K.; Takeda, M.; Porter, R. S. *Macromolecules* **1988**, *21*, 470–477.
- (29) Peguy, A.; Manley, R. S. J. *Polym. Commun.* **1984**, *25*, 39–42.
- (30) Kim, B. S.; Porter, R. S. *Macromolecules* **1985**, *18*, 1214–1217.
- (31) Clark, E. S.; Scott, L. S. *Polym. Eng. Sci.* **1974**, *14*, 682–686.
- (32) He, T.; Porter, R. S. *Polymer* **1987**, *28*, 946–950.
- (33) Schaefer, D.; Spiess, H. W.; Suter, U. W.; Fleming, W. W. *Macromolecules* **1990**, *23*, 3431–3439.
- (34) Schmidt-Rohr, K.; Spiess, H. W. *Macromolecules* **1991**, *24*, 5288–5293.
- (35) Schmidt-Rohr, K.; Spiess, H. W. *Multidimensional Solid-State NMR and Polymers*; Academic Press: London, 1994.
- (36) Hu, W.-G.; Boeffel, C.; Schmidt-Rohr, K. *Macromolecules* **1999**, *32*, 1611–1619.
- (37) deAzevedo, E. R.; Hu, W.-G.; Bonagamba, T. J.; Schmidt-Rohr, K. *J. Am. Chem. Soc.* **1999**, *121*, 8411–8412.
- (38) Miyoshi, T.; Pascui, O.; Reichert, D. *Macromolecules* **2004**, *37*, 6460–6471.
- (39) Hu, W. G.; Schmidt-Rohr, K. *Acta Polym.* **1999**, *50*, 271–285.
- (40) Natta, G.; Corradini, P. *Nuovo Cimento Suppl.* **1960**, *15*, 40–51.
- (41) Mencik, Z. *J. Macromol. Sci., Phys.* **1972**, *B6*, 101–115.
- (42) Hikosaka, M.; Seto, T. *Polym. J.* **1973**, *5*, 111–127.
- (43) Guerra, G.; Petraccone, V.; Corradini, P.; De Rosa, C.; Napolitano, R.; Pirozzi, B.; Giunchi, G. *Polym. Sci. Polym. Phys.* **1984**, *22*, 1029–1039.
- (44) Naiki, M.; Kikkawa, T.; Endo, Y.; Nozaki, K.; Yamamoto, T.; Hara, T. *Polymer* **2000**, *42*, 5471–5477.
- (45) Bunn, A.; Cudby, M. E. A.; Harris, R. K.; Packer, K. J.; Say, B. J. *Polymer* **1982**, *23*, 694–698.
- (46) Bennett, A. E.; Rienstra, C. M.; Auger, M.; Lakshmi, K. V.; Griffin, R. G. *J. Chem. Phys.* **1995**, *103*, 6951–6958.
- (47) Miyoshi, T.; Mamun, A.; Hu, W. *J. Phys. Chem. B* **2010**, *114*, 92–100.
- (48) Li, Z.; Miyoshi, T.; Sen, M. K.; Koga, T.; Otsubo, A.; Kamimura, A. *Macromolecules* **2013**, *46*, 6507–6519.
- (49) Takahashi, T.; Kawashima, H.; Sugisawa, H.; Toshihide, B. *Solid State Nucl. Magn. Reson.* **1999**, *15*, 119–123.
- (50) Clauss, J.; Schmidt-Rohr, K.; Spiess, H. W. *Acta Polym.* **1993**, *44*, 1–17.
- (51) Hu, W. G.; Schmidt-Rohr, K. *Polymer* **2000**, *41*, 2979–2987.
- (52) Litvinov, V. M.; Xu, J.; Melian, C.; Demco, D. E.; Möller, M.; Simmelink, J. *Macromolecules* **2011**, *44*, 9254–9266.
- (53) Buda, A.; Demco, D. E.; Blumich, B.; Litvinov, V. M.; Penning, J. P. *ChemPhysChem* **2004**, *5*, 876–883.
- (54) Pasquini, N. *Polypropylene Handbook*, 2nd ed.; Carl Hanser Verlag: Munich, 2005.
- (55) VanderHart, D. L.; Alamo, R. G.; Nyden, M. R.; Kim, M. H.; Mandelkern, L. *Macromolecules* **2000**, *33*, 6078–6093.
- (56) Vincent, P. I. *Polymer* **1960**, *1*, 7–19.
- (57) Meinel, G.; Peterlin, A. *J. Polym. Sci., Polym. Phys.* **1971**, *9*, 67–83.
- (58) Popli, R.; Madelkern, L. *J. Polym. Sci., Polym. Phys.* **1987**, *25*, 441–483.
- (59) Lucas, J. C.; Failla, M. D.; Smith, F. L.; Manderkern, L. *Polym. Eng. Sci.* **1995**, *35*, 1117–1123.
- (60) Hong, Y.; Miyoshi, T. *ACS Macro Lett.* **2013**, *2*, 501–505.
- (61) Cheng, S. Z. D.; Janimak, J. J.; Zhang, A.; Hsieh, E. T. *Polymer* **1991**, *32*, 648–655.
- (62) Mowery, D. M.; Harris, D. J.; Schmidt-Rohr, K. *Macromolecules* **2006**, *39*, 2856–2865.
- (63) Wunderlich, B. *Macromolecular Physics*; Academic Press: New York, 1980; Vol. 3.
- (64) Yamada, K.; Hikosaka, M.; Toda, A.; Yamazaki, S.; Tagashira, K. *Macromolecules* **2003**, *36*, 4790–4801.